buildings

MDPI

Article

A Restoring Force Correction Model for Enveloped Steel Jacket-Confined Seismic-Damaged Rectangular Recycled Aggregate Concrete-Filled Steel Tubular Columns

Jun Yan [1], Sheng Peng [2,3,4,5], Naimeng Chen [5,*], Tianlei Wang [2] and Yang Song [5,*]

[1] Wuhan Bohong Construction Group Co., Ltd., Wuhan 430050, China; yan_jun_@sina.com
[2] Tianjin Key Laboratory of Building Green Functional Materials, Tianjin Chengjian University, Tianjin 300384, China
[3] State Key Laboratory of Precision Blasting, Jianghan University, Wuhan 430056, China
[4] Hubei Key Laboratory of Blasting Engineering, Jianghan University, Wuhan 430056, China
[5] School of Urban Construction, Wuhan University of Science and Technology, Wuhan 430065, China
* Correspondence: chennaimeng0107@163.com (N.C.); songyang0506@wust.edu.cn (Y.S.)

Abstract: In order to establish a suitable restoring force correction model for enveloped steel jacket (ESJ)-confined seismic-damaged rectangular recycled aggregate concrete-filled steel tubular (RRACFST) columns, based on experimental research, a study of the seismic performance and parameters of ESJ-confined seismic-damaged RRACFST columns was carried out. The restoring force theory, model test, and OpenSees simulation of ESJ-confined seismic-damaged RRACFST columns were conducted. Firstly, a trilinear model of the skeleton curve and a suitable restoring force model for ESJ-confined seismic-damaged RRACFST columns were established. The results were compared with the model test results, and it was found that the two results had good consistency. Secondly, the initial damage of the RRACFST column was simulated by the reducing material properties method, and a correct numerical model for ESJ-confined seismic-damaged RRACFST columns was proposed. The influence mechanism of seismic parameters of the RRACFST column was clarified. Finally, the seismic parameter combination with the best seismic performance for ESJ-confined seismic-damaged RRACFST columns was established; namely, the replacement rate of recycled coarse aggregate is 50%, the concrete strength is C40, the axial compression ratio is 0.3, the strength of the rectangular steel tube is Q345, the wall thickness of the steel tube is 4 mm, and the slenderness ratio is 7.5.

Keywords: enveloped steel jacket (ESJ)-confined; rectangular recycled aggregate concrete-filled steel tubular (RRACFST) column; restoring force correction model; OpenSees simulation; seismic performance

check for updates

Citation: Yan, J.; Peng, S.; Chen, N.; Wang, T.; Song, Y. A Restoring Force Correction Model for Enveloped Steel Jacket-Confined Seismic-Damaged Rectangular Recycled Aggregate Concrete-Filled Steel Tubular Columns. *Buildings* **2024**, *14*, 3521. https://doi.org/10.3390/buildings14113521

Academic Editor: Andreas Lampropoulos

Received: 9 October 2024
Revised: 29 October 2024
Accepted: 3 November 2024
Published: 4 November 2024

Copyright: © 2024 by the authors. Licensee MDPI, Basel, Switzerland. This article is an open access article distributed under the terms and conditions of the Creative Commons Attribution (CC BY) license (https://creativecommons.org/licenses/by/4.0/).

1. Introduction

In order to solve the problem of the increasing use of resources and to meet the strategic requirements of sustainable development, recycled aggregate concrete (RAC) is widely used in engineering structures [1]. RAC is made by crushing, cleaning, grading, and mixing waste concrete materials from discarded construction waste according to certain proportions and replacing natural aggregates with these mixed aggregates. Although RAC materials fully utilize the recycling of discarded solid materials to solve the problem of resource waste [2,3], the process of reprocessing the aggregates inevitably affects the material properties of concrete, resulting in a significant performance gap between RAC and natural concrete. In order to avoid this situation, recycled aggregate concrete-filled steel tubular (RACFST) structures are used in construction projects.

Concrete-filled steel tubular (CFST) structures have been used in housing, bridges, water conservancy, port structures, and other civil engineering projects. CFST structures save the use of natural aggregates and improve the bearing capacity and seismic performance

of such structures through the restraining effect of steel tubes on RAC [4]. However, it is widely believed that the performance of RAC is inferior compared to natural aggregate concrete (NAC). To compensate for this deficiency, scholars have conducted research on the repair and reinforcement of these structures during use, as well as seismic performance testing and simulation [5,6]. Finite element analysis is a common research method. Di Cesare et al. [7] simulated the seismic performance of a composite reinforced concrete truss (CRCT) beam and a reinforced concrete (RC) or concrete-filled tube (CFT) column through two simple modeling methods using Sap2000 software V25.0.0, and the experimental results were consistent with the simulation results. Colajanni et al. [8,9] proposed an improved device to reduce the friction of hybrid steel-trussed concrete beams (HSTCBs) and standard RC column joints, with a pushover analysis and nonlinear time history of the simple two layers and two spans of the device to prove the feasibility of the device. Dong et al. [10] used OpenSees fiber elements to establish a RACFST column model and achieved good consistency between the experimental results and predicted results. Liu et al. [11] applied OpenSees to study the seismic performance of irregular cross-section space frames and compared the results with the experimental values to prove the feasibility of the software. At the same time, they analyzed the influence of load direction, the axial compression ratio, and the column flange length-to-width ratio on the seismic performance of the structure. Bicici et al. [12] proposed an easy-to-use shear displacement model in OpenSees software 3.3.0, which can be used to detect cyclic shear responses through test results. Liu et al. [13] developed a nonlinear elastic–plastic model for the seismic performance of concrete-filled steel tubular arch structures using OpenSees and proved its feasibility through experiments.

At present, common reinforcement methods mainly include increasing the sectional area, replacing the concrete structure, applying external prestressing, bonding the steel sections, bonding fiber composite materials, and bonding steel plates [14]. The ESJ-confined method has good construction performance, and it is easy to employ materials from a wide range of sources. It is a very effective seismic reinforcement method and has been widely used in structural repair and reinforcement projects [15–18]. Xu et al. evaluated the seismic performance of four ESJ-confined steel-reinforced concrete (SRC) columns, using non-destructive unreinforced, non-destructive reinforced, moderate pre-damage reinforced, and severe pre-damage reinforced columns [19]. The experimental results showed that compared to unreinforced components, ESJ-confined columns had fewer cracks and could effectively improve seismic performance. Aldhafairi et al. evaluated the parameters of ESJ-confined components, including changing the size of the angle steel, the welding method of angle steel, and the angle of the top corner. They proposed a more suitable reinforcement method for the structure that is beneficial for the application of ESJ-confined components [20]. Peng et al. designed ESJ-confined components, assuming that other parameters remained unchanged, and analyzed their failure phenomena, hysteresis curves, skeleton curves, strength degradation, stiffness degradation, ductility, and energy dissipation performance [21]. The results showed that ESJ-confined RACFST columns had good dissipation capacity and bearing capacity. Trapani et al. obtained the optimal configuration structure of ESJ-confined RC based on genetic algorithms in the OpenSees fiber model [22]. According to the above research, there is a lack of numerical simulation studies on the seismic performance of ESJ-confined seismic-damaged RRACFST columns based on OpenSees software.

The restoring force model is one of the most important methods for studying the elastic-plastic time-history analysis of structures, providing an important theoretical basis for ensuring the measures of buildings under earthquake action. For the establishment of the restoring model of steel tube concrete structural components, most of them refer to RC components. Xue et al. [23] proposed a four-line restoring force model for steel-reinforced RAC and conducted extensive research on the restoring force model using ABAQUS software 6.14.2. Han et al. [24] conducted experimental research on concrete-filled double-skin steel tubular beam columns and established a restoring model for the relationship between moment (M) and curvature (φ) response, lateral load (P), and lateral displacement

(Δ). Peng et al. [25] created a restoring force model for seismic-damaged RACFST columns confined with CFRP, using OpenSees software. Wang et al. [26] conducted a restoring force model for composite frames with concrete-confined CFST columns, based on OpenSees parametric analysis. Wu et al. proposed a trilinear restoring model for H-shaped steel-concrete composite joints through numerical regression analysis [27]. Yun et al. submitted a new restoring force model for the prefabricated self-centering beam to the column, based on an experiment [28]. The current restoring force model mainly focuses on RC structures and joint structures, according to the existing research, and further research is needed for a restoring force model of ESJ-confined seismic-damaged RRACFST columns.

In addition, research on the restoring force model, numerical simulation, and seismic performance parameters of ESJ-confined seismic-damaged RRACFST columns has not yet been covered. Based on existing experimental data, this article establishes a restoring force model through a skeleton curve theoretical model and the stiffness degradation law. The results showed that the restoring force model agreed well with the experimental data, proving the feasibility of the restoring force model. At the same time, the model was established using OpenSees finite element software and fitted with the experimental data; the fitting results were good, which verified the feasibility of OpenSees software. Subsequently, through OpenSees, further research was conducted on the influence of parameters on pre-damaged specimens, and the optimal seismic parameter combination for the seismic performance of RRACFST columns was given, providing a theoretical basis and evidence for the seismic performance of ESJ-confined seismic-damaged RRACFST columns.

2. Experimental Overview

2.1. Specimen Design

In order to study the influence of the ESJ-confined method and seismic damage on the seismic performance of RRACFST columns, the authors of Reference [21] designed and fabricated four column models with a scale ratio of 1:2. The external dimensions of the columns were 200 m × 200 mm × 4 mm, with a height of 1500 m. All steel materials used were of Q235B-grade steel, with a steel ratio of 8.5% in the steel tube section. The steel tube was filled with RAC with a replacement rate of 50% and a strength grade of C40. The angle steel used was L63 mm × 4 mm, and the batten plate used was 86 mm × 50 mm × 4 mm. The angle steel, batten plate, and concrete were filled with steel-bonding glue, and the spacing between the batten plates was 100 mm. The height of the reinforced area was 500 mm. The specific specimen parameters are shown in Table 1. Tables 2 and 3 show the material properties of the steel tubes and the RAC. Figure 1 shows the structure of the ESJ-confined specimen. In this study, "-T" represents the measured value of the specimen, such as "RRACFST-0-T", and "-S" represents the simulated value of the specimen, such as "RRACFST-0-S".

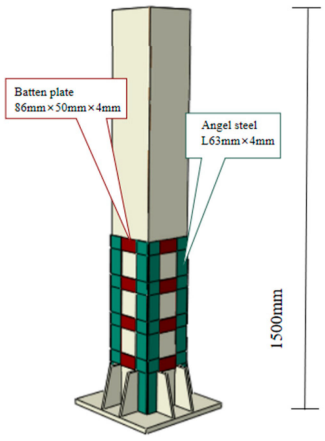


Figure 1. Diagram of the ESJ-confined specimen.

Table 1. Specimen design.

Specimen	Damage Degree	Axial Pressure Ratio/kN	Reinforcement Method	Pre-Damaged Displacement/mm	Pre-Damaged Displacement Angle
RRACFST-0	-	0.32 (500)	-	0	-
RRACFST-1	-	0.32 (500)	ESJ	0	-
RRACFST-2	moderate earthquakes	0.32 (500)	ESJ	12	1/50
RRACFST-3	large earthquake	0.32 (500)	ESJ	24	1/100

Table 2. Material properties of steel.

Material	Strength Grade	Steel Thickness t/mm	Yield Strength f_y/MPa	Tensile Strength f_t/MPa	Elastic Modulus E_s/MPa
steel pipe	Q235B	4	212	446	2.02×10^5
angle steel	Q235B	4	242	419	1.93×10^5
batten plate	Q235B	4	225	406	2.05×10^5
stiffener plate	Q235B	10	293	462	1.92×10^5
bottom plate	Q235B	20	244	424	2.01×10^5

Table 3. Material properties of RAC.

Strength Grade	Particle Size/mm	Measured Compressive Strength/MPa	Water–Cement Ratio	Amount per Cubic m/kg				
				Cement	Water	Sand	Natural Aggregate	Recycled Aggregate
C40	5–25	40.12	0.48	420	205	561	569.3	569.3

2.2. Loading Condition and Pre-Damage Method

Quasi-static loading uses an electro-hydraulic servo press system to simulate the seismic damage of steel tube RAC column structures. The constant vertical load was applied at the top of the column by a hydraulic jack, ensuring that the loading end of the specimen moved with the electric servo-hydraulic actuator and the sliding trolley connected the specimen to the reaction frame beam. At the same time, the column base plate was connected to the base by eight M30 friction-type high-strength bolts [25]. The horizontal loading used displacement control, and, before the specimen yielded, each level of displacement peak was applied step by step according to the lateral displacement increment Δ/L = 0.25%, 0.5%, 0.75%, and 1.0%. Each level of the displacement cycle was repeated once until the loading value reached the yield displacement. The loading system followed the specifications of the "Specification for the seismic test of buildings" (JGJ/T 101-2015) [29]. After the specimen yielded, it was loaded step by step according to the integer multiples of the yield displacement, with three cycles per displacement, until it dropped below 85% of the peak load or the column deformation became too large, and the test loading was stopped. The test referred to the specifications of the "Code for seismic design of buildings" (GB 50011-2010) to simulate the pre-damage level [30]. A displacement angle of 1/100 was adopted to simulate moderate pre-damage during moderate earthquakes, and a displacement angle of 1/50 was adopted to simulate severe pre-damage during major earthquakes. The axial compression ratio was 0.32. The specific loading system is shown in Figure 2, and the test loading device is shown in Figure 3. The actual experimental setup and results diagram are shown in Figures 4 and 5.

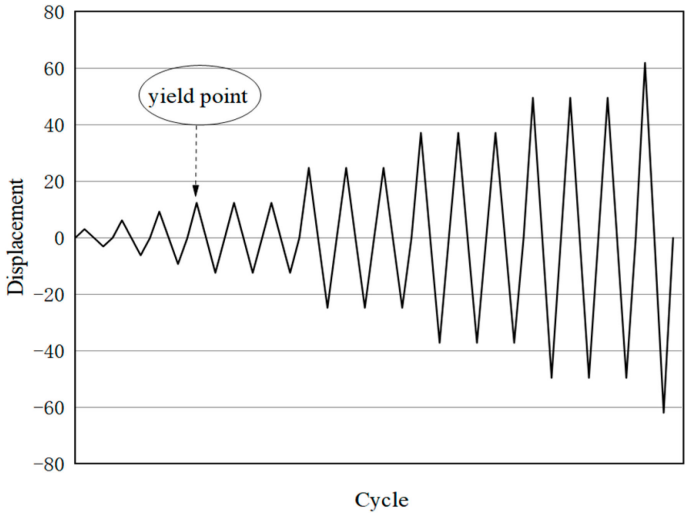


Figure 2. Displacement history.

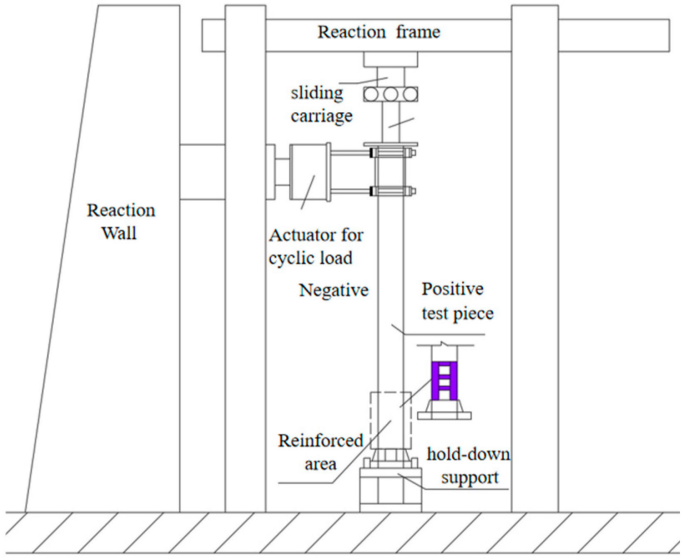


Figure 3. Schematic diagram of the loading device.

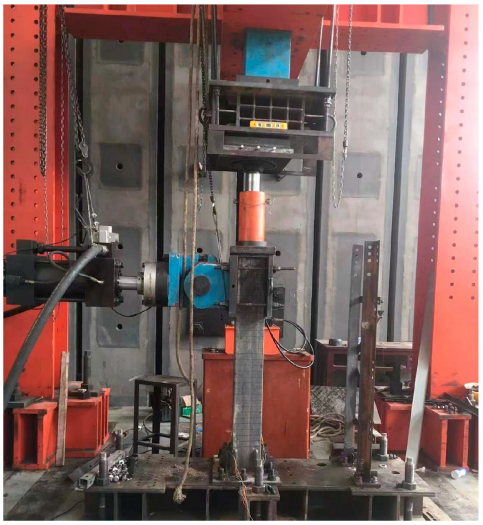


Figure 4. Actual experimental setup.



Figure 5. Images of the actual experimental results.

3. Restoring Force Correction Model of ESJ-Confined Seismic-Damaged RRACFST Columns

3.1. Simplified Theoretical Model of the Skeleton Curve

The skeleton curve reflects the degradation performance and ductility characteristics of the structure at different stages under low reversed cyclic loading. Hu et al. [31] built a skeleton curve model with yield, peak, and softening points. Du et al. [32] suggested that the trilinear skeleton curve can intuitively reflect the linear relationship between displacement and load, and also fits well with the skeleton curve of CFST columns. Hu et al. [33] applied the Pinching4 model to calculate the skeleton curves, which also gave good results. Based on experimental data [21], the yield point, the peak point, and the damage point were characterized clearly; to facilitate the calculation, this article adopted a test fitting method to simplify the skeleton curve into a trilinear model, and the authors performed dimensionless coordinate transformation on the displacement-load data of four RRACFST columns. By selecting the characteristic points and calculating the average value, the dimensionless displacement and load data of the characteristic points were determined and obtained. The theoretical model of the skeleton curve was fitted through data fitting [25]. The results of dimensionless processing for the characteristic points of the test specimens are shown in Table 4. The theoretical trilinear model of the skeleton curve is shown in Figure 6, and the equations for each stage of the model are shown in Table 5. Δ_y, Δ_m, and Δ_u are the displacements of the yield point, peak point, and damage point. P_y, P_m and P_u are the load of the yield point, peak point, and damage point. A(A′), B(B′), and C(C′) indicate the positive (negative) relative damage point, relative peak point, and relative yield point of the specimen, respectively. OC is the elastic–plastic stage, CB is the plastic stage, and BA is the damage stage.

Table 4. Dimensionless load and displacement of the characteristic points of the measured skeleton curve.

Specimen	Load Direction	Yield Point		Peak Point		Damage Point	
		P_y/P_m	Δ_y/Δ_m	P_m/P_m	Δ_m/Δ_m	P_u/P_m	Δ_u/Δ_m
RRACFST-0	Positive	0.790	0.357	1.000	1.000	0.905	1.339
	Negative	−0.848	−0.396	−1.000	−1.000	−0.849	−1.588
RRACFST-1	Positive	0.804	0.371	1.000	1.000	0.937	1.361
	Negative	−0.712	−0.329	−1.000	−1.000	−0.902	−1.298
RRACFST-2	Positive	0.845	0.336	1.000	1.000	0.922	1.293
	Negative	−0.721	−0.309	−1.000	−1.000	−0.820	−1.369
RRACFST-3	Positive	0.783	0.351	1.000	1.000	0.863	1.404
	Negative	−0.796	−0.338	−1.000	−1.000	−0.836	−1.409

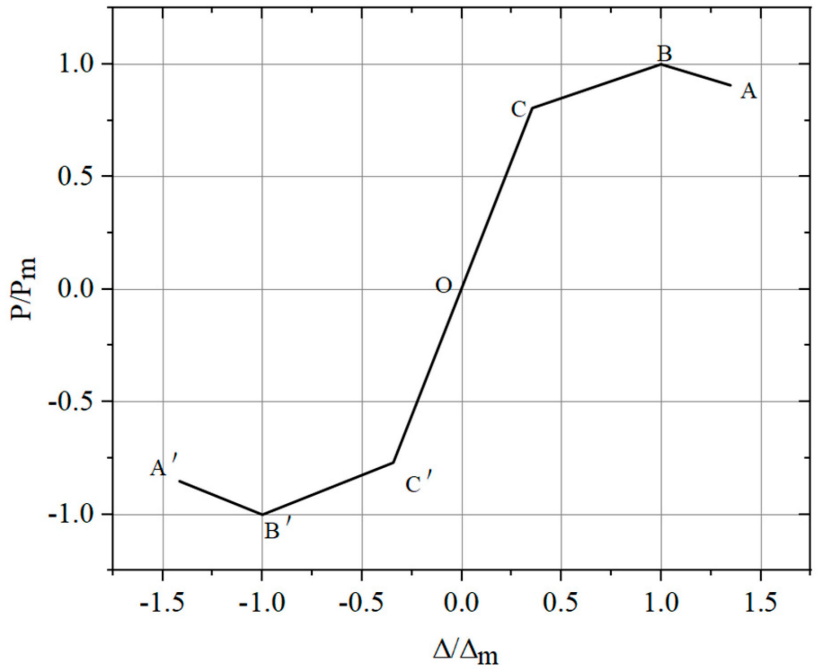


Figure 6. Theoretical skeleton curve model.

Table 5. Equations for each stage of the theoretical skeleton curve.

Segment	Equation	Segment	Equation
OC	$P_y/P_m = 2.276\Delta_y/\Delta_m$	OC′	$P_y/\lvert P_m\rvert = 2.242\Delta_y/\Delta_m$
CB	$P_y/P_m = 0.700 + 0.300\Delta_y/\Delta_m$	C′B′	$P_y/\lvert P_m\rvert = 0.649 + 0.351\Delta_y/\Delta_m$
BA	$P_y/P_m = 1.266 - 0.266\Delta_y/\Delta_m$	B′A′	$P_y/\lvert P_m\rvert = 1.356 - 0.356\Delta_y/\Delta_m$

The displacement data of the characteristic points obtained from the test were substituted into the above expression to obtain the theoretical load values of the characteristic points. Comparing the displacement-load values obtained from the test of each characteristic point with the displacement-load values of the model, it can be observed that the results obtained from the theoretical model and the experimental model were basically consistent, which indicated that the obtained trilinear model of the skeleton curve could be used to predict the skeleton curve of seismic-damaged ESJ-confined RRACFST columns. Du et al. [31] obtained similar results. The comparison diagram of the experimental and model skeleton curves is shown in Figure 7.

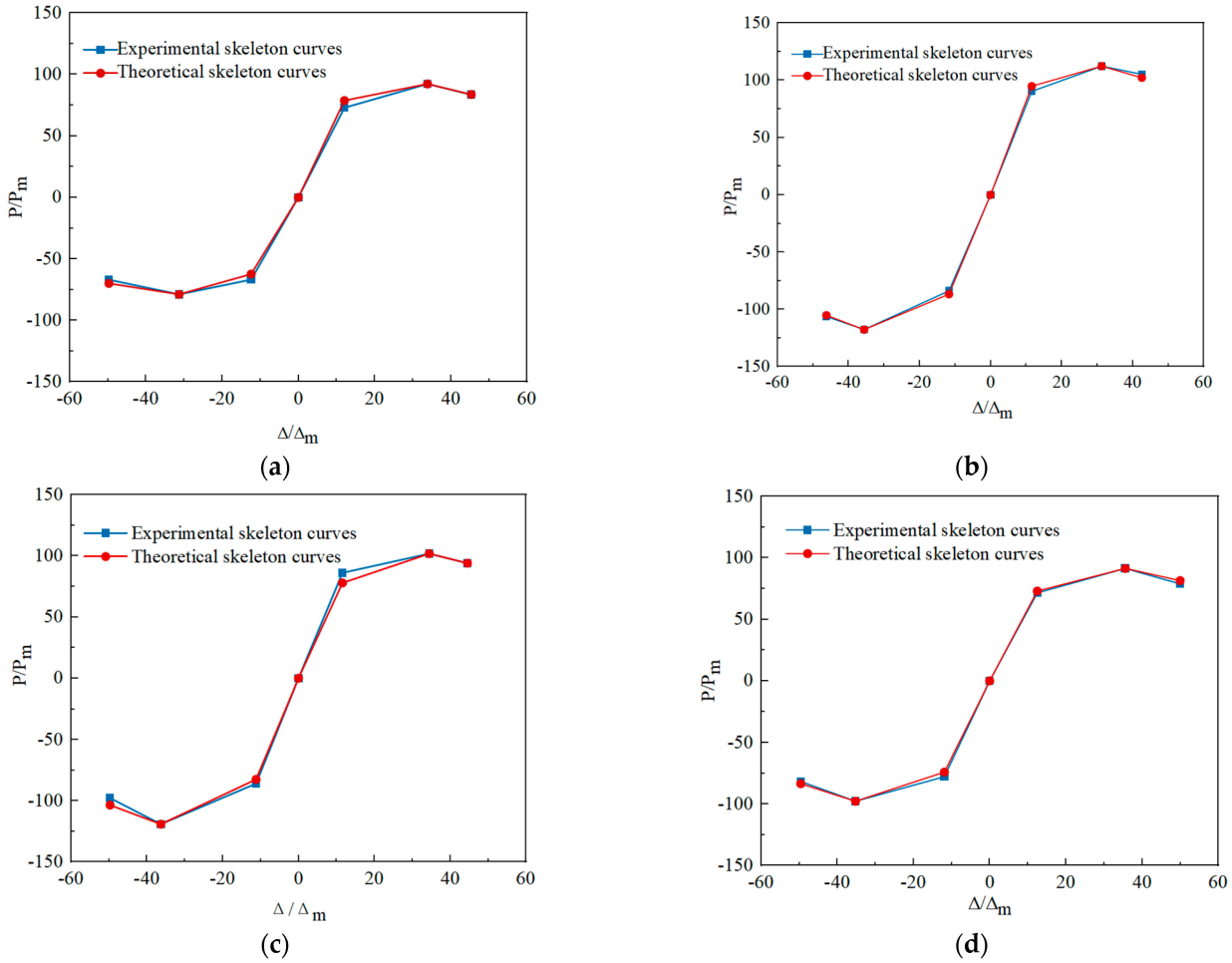


Figure 7. Comparison of the experimental and theoretical skeleton curves. (**a**) RRACFST-0; (**b**) RRACFST-1; (**c**) RRACFST-2; (**d**) RRACFST-3.

3.2. Stiffness Degradation

The stiffness degradation curve describes the damage degree of the model and can be used to establish the restoring force model of the component. According to the experimental data in the literature [21], the unloading stiffness of steel tube RAC columns degrades with an increase in displacement. Peng et al. [25] obtained the same laws. The positive stiffness degradation curve law is shown in Figures 8 and 9, and the negative stiffness degradation curve law is shown in Figures 10 and 11. By analyzing the experimental data of positive and negative unloading stiffness K and the positive and negative yield point laws, the initial stiffness K_0 was obtained. The unloading stiffness was normalized with the initial stiffness and cyclic displacement, respectively. Referring to Equation (1), the obtained parameters were subjected to exponential linear regression to fit the positive and negative unloading stiffness degradation curves. The positive and negative unloading regression equations are, respectively, expressed as Equations (2) and (3), while the positive and negative loading regression equations are expressed as Equations (4) and (5).

$$y = ae^{-x/b} + c \tag{1}$$

$$\frac{K}{K_0} = 2.411e^{-\frac{\Delta}{0.780\Delta_m}} + 0.6655 \; R^2 = 0.96417 \tag{2}$$

$$\frac{K}{K_0} = 2.373e^{-\frac{\Delta}{0.813\Delta_m}} + 0.4647 \; R^2 = 0.98552 \tag{3}$$

$$\frac{K}{K_0} = 1.735e^{-\frac{\Delta}{0.514\Delta_m}} + 0.1976 \; R^2 = 0.98783 \tag{4}$$

$$\frac{K}{K_0} = 1.305e^{-\frac{\Delta}{0.698\Delta_m}} + 0.1343 \; R^2 = 0.96063 \tag{5}$$

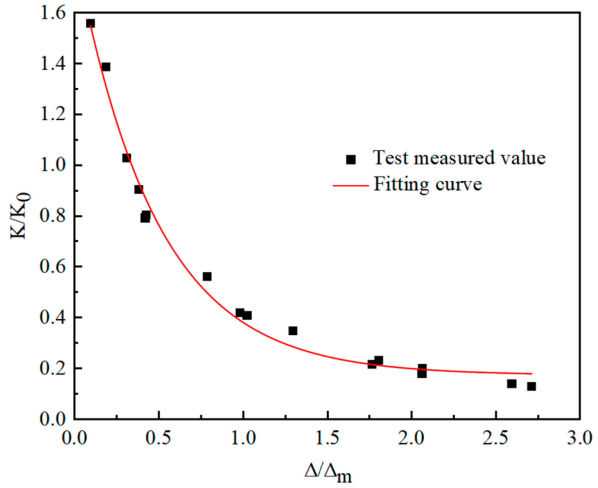


Figure 8. Positive loading stiffness degradation curve.

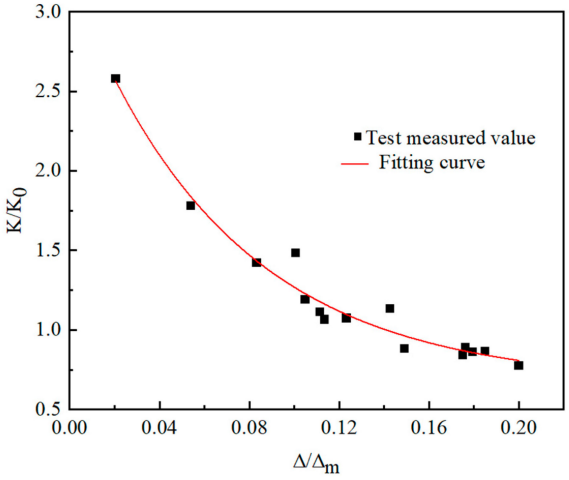


Figure 9. Positive unloading stiffness degradation curve.

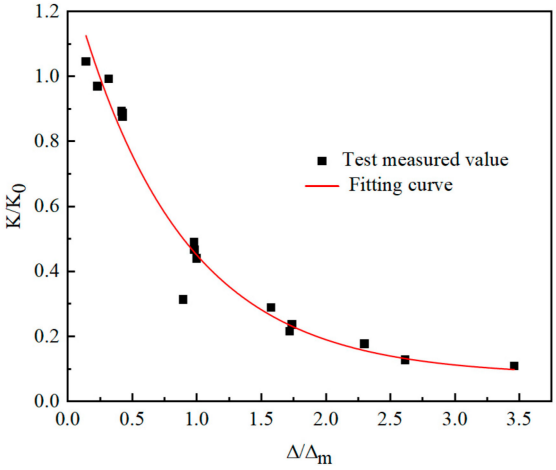


Figure 10. Negative loading stiffness degradation curve.

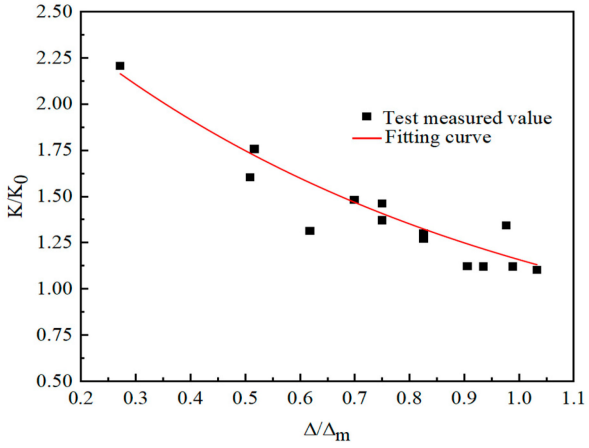


Figure 11. Negative unloading stiffness degradation curve.

3.3. Proposing and Validating the Hysteretic Model

The hysteretic model can accurately and conveniently predict the seismic performance of structures. The hysteretic models established by Rodrigues et al. [34], Xiao et al. [35], and Sivaselvan et al. [36] include bilinear, trilinear, and multilinear types. The hysteretic model was established based on experimental data and theoretical models of the above skeleton curves, combined with positive and negative unloading stiffness degradation laws. The model in this article uses a trilinear model, as shown in Figure 12. From the hysteresis curve, it can be seen that both positive and negative loading points then point to a fixed point under each cyclic displacement. In order to facilitate the use of the hysteretic model, this fixed point is defined as the positive and negative yield points. When the specimen reaches the auxiliary amplitude values in both positive and negative directions, the bearing capacity suddenly drops, even reaching a linear downward trend. The selection of positive and negative displacement amplitude values is determined by analyzing the data and selecting 0.6 and −0.6, respectively. Peng et al. [25] also reached similar conclusions. The softening point treatment is based on Reference [37], where the ordinate of each softening point is taken as 0.2 times the displacement amplitude bearing capacity. After reaching the peak point, the ordinate of each softening point is taken as 0.4 times the displacement amplitude bearing capacity.

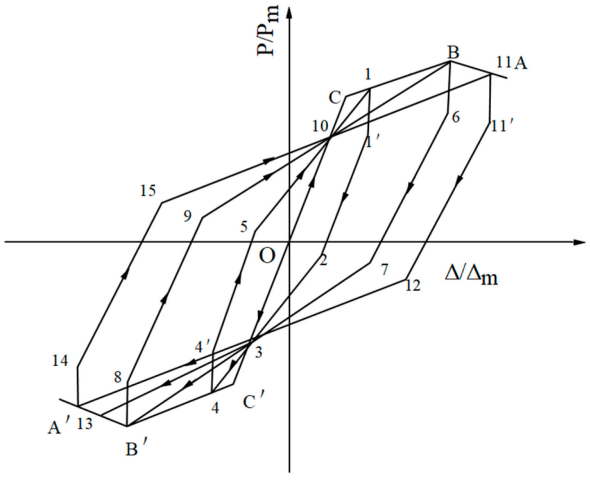


Figure 12. The restoring force model.

The hysteresis rule of the hysteretic model is described as follows:

(1) Before the positive and negative loading of the RRACFST column reaches 0.6 and 0.6′, respectively, the loading and unloading paths are positioned along the elastic stage,

namely, the OC and OC′ segments in Figure 12. During this stage, the unloading stiffness remains constant and is considered the initial stiffness.

(2) When the load on the RRACFST column reaches the yield point and the RRACFST column suddenly changes to between 0.6 and the yield point, the loading path for loading and unloading follows the path C-B-A. When unloading at point 1, it suddenly changes to point 1′, pointing to point 2, unloading line 1′2, and reversing the loading through point 3, pointing to point 4. Reversing the unloading changes from point 4 to point 4′, pointing to point 5, and the unloading path is 4′5. When continuing to load points 10 and 1, the cyclic path is 1-1′-2-3-4-4′-5-10-1.

(3) When the column reaches the ultimate load, the unloading line is B-6-7, and it continues to load to point 3. If the reverse loading does not reach the ultimate load, it points to extreme point B′. It continues to reverse unload at point B′, then suddenly changes to 8, unloads to 9, and points to 10 to B. The cycle path is B-6-7-3-B′-8-9-10-B. The BA damaged section 11 points to unloading. Mutation to the 11′ unloading line is 11′12, then it points to 3 and then to point A′, reverse unloading to point 14, and then points to point 15. It continues to load from point 15 to point 10 to point 11. The cycle path is 11-11′-12-3-A′-14-15-10-11. If the reverse loading exceeds the limitation point, it points to point 13 of the damaged section A′B′. The above cycle is then repeated.

(4) The results of the hysteretic model calculation of the test specimens were compared with the results measured from the test data. The results were in good agreement, as shown in Figure 13, proving that this hysteretic model can better represent the relationship between displacement and load, and is suitable for the study of specimens of ESJ-confined seismic-damaged RRACFST columns.

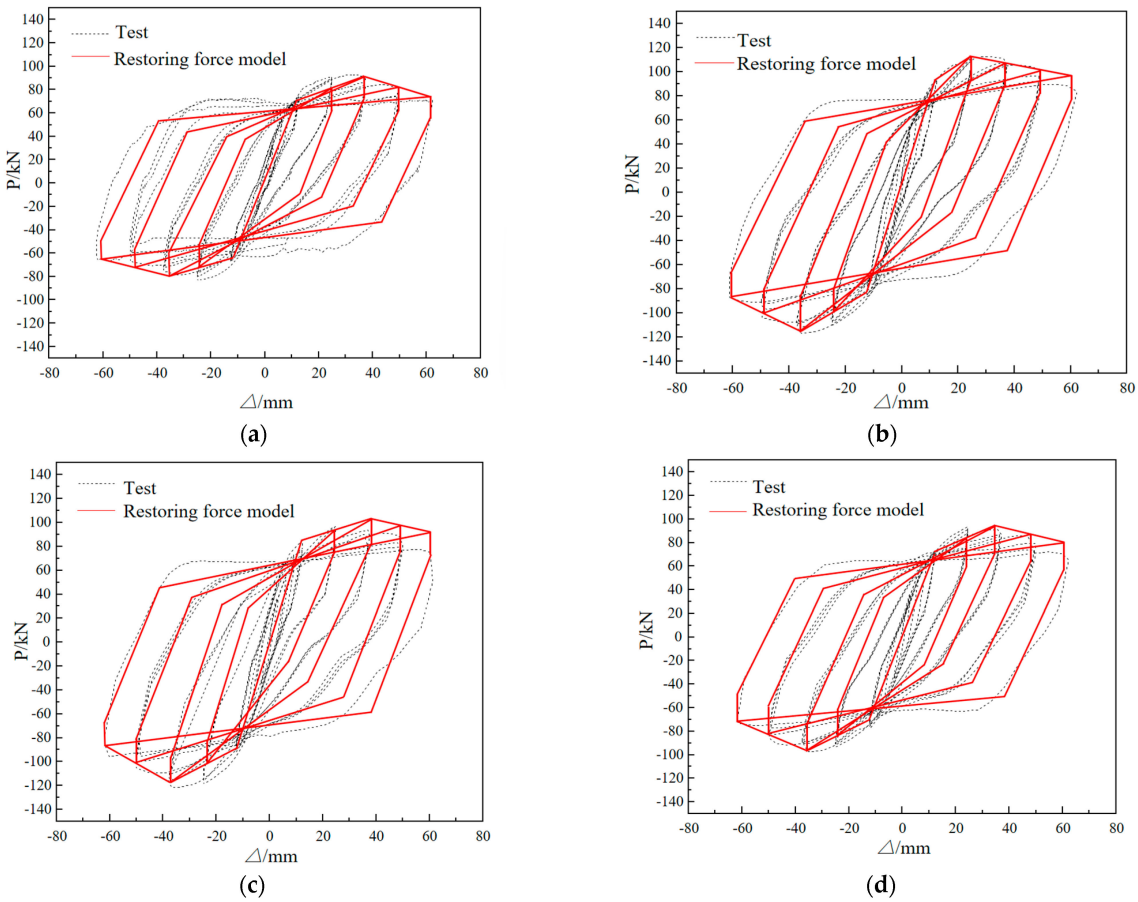


Figure 13. Comparison of the restoring force model and test hysteresis curves. (**a**) RRACFST-0; (**b**) RRACFST-1; (**c**) RRACFST-2; (**d**) RRACFST-3.

4. OpenSees Application

4.1. The Material Constitutive Model

The concrete constitutive model Concrete 02 in the OpenSees software was selected for the RAC structure model [25]. This constitutive relationship is based on the Kent–Park model and works by changing the peak stress-strain magnitude and softening slope of the concrete skeleton curve at the compression end, taking into account the improvements in the strength and ductility of the core area concrete due to lateral constraints, as shown in Figure 14. F_c is concrete compressive strength, f_t is the tensile strength, and f_{20} is the crushing strength. E_0, ε_t, ε_{20} is the concrete strain of f_c, f_t, f_t. E_0 is the elastic modulus. E_{ts} is the tension softening stiffness. The relevant values can be obtained from experimental data. The formula for calculating the compressive strength of concrete is shown in Equations (6)–(12). According to the characteristics of the Kent–Park model, the tensile segment is simplified to a straight line. The rectangular steel tube constitutive model Steel 02 (Giuffre–Menegotto–Pinto steel constitutive model) [38] was selected in the OpenSees software. This model can better reflect the Bauschinger effect of steel, with its simple calculation formulas, fast calculation efficiency, and high simulation agreement. It fully considers the impact of strain hardening on steel, as shown in Figure 15. E_y is yield strength, σ_y is the strain of ε_y, E_1 is the initial elastic modulus, and b is the steel hardening factor. The formula Is as shown In Equations (13)–(17). The yield strength and elastic modulus of steel can be input according to the test results. The control parameter R_0 for the transition from the elastic to the plastic stage in OpenSees was between 10 and 20. Combined with the test results, all specimens had a value of 18; cR_1 and cR_2 were taken as 0.925 and 0.15, respectively [25].

$$f_{cc} = Kf_c \tag{6}$$

$$K = 1 + 0.5k_e\xi \tag{7}$$

$$k_e = f(n)(1 - \psi) \tag{8}$$

$$f(n) = \left(n^2 - 4\right)\left(n^2 + 20\right) \tag{9}$$

$$\alpha = \frac{kr}{r - 1 + k'} \tag{10}$$

$$r_0 = \frac{E_c}{E_c - f_c/\varepsilon_c} \tag{11}$$

$$r = r_0\frac{f_c}{f_{cc}} = \frac{2}{K} \tag{12}$$

Here, K is the proportional coefficient of intensity, ξ is the constraint effect coefficient, r is the curve effect coefficient, k_e is the steel tube cross-section influence coefficient, and n is the number of tube cross-section-shaped sides. The strain ε_{cc} corresponding to f_{cc} is $\varepsilon_{cc} = Kf_{cc}$. The formula for calculating the crushing strength is $\varepsilon_{cu} = K\varepsilon_{cc}$, $f_{cu} = \alpha f_{cc}$.

$$\sigma^* = \mathrm{b}\varepsilon + \frac{(1 - \mathrm{b})\varepsilon^*}{\left(1 + \varepsilon^{*\mathrm{R}}\right)^{1/\mathrm{R}}} \tag{13}$$

$$\sigma^* = \frac{\sigma - \sigma_\mathrm{r}}{\sigma_0 - \sigma_\mathrm{r}} \tag{14}$$

$$\varepsilon^* = \frac{\varepsilon - \varepsilon_\mathrm{r}}{\varepsilon_0 - \varepsilon_\mathrm{r}} \tag{15}$$

$$R = R_0 - \frac{a\zeta}{a_2 + \zeta} \tag{16}$$

$$\zeta = \left|\frac{\varepsilon_\mathrm{m} - \varepsilon_0}{\varepsilon_y}\right| \tag{17}$$

Here, σ^* and ε^* are the stress and strain normalized treatment values. R is the transition curve curvature line. Σ_0 and ε_0 are the corresponding values of the outer envelope at the yield point. Σ_r and ε_r are the corresponding values at the reverse loading point, respectively. Z is the maximum strain parameter. R_0 is the initial loading curve curvature factor.

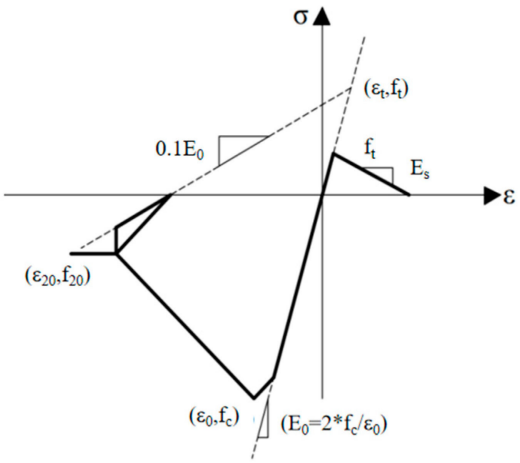


Figure 14. The Kent–Park concrete constitutive model.

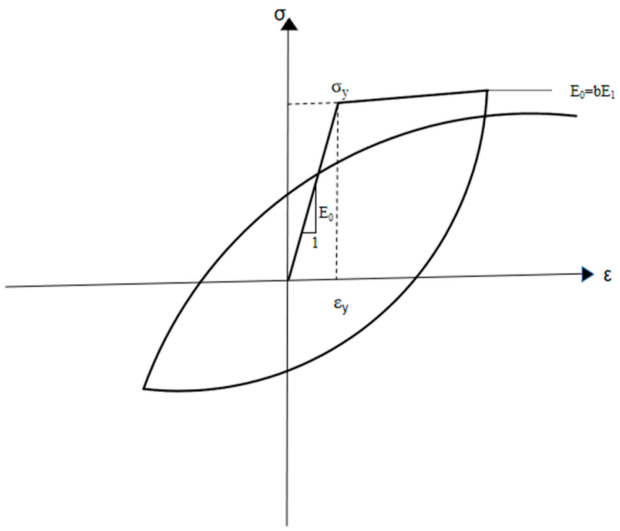


Figure 15. Steel constitutive model.

4.2. Modeling Unit Types and Divisions

The model section uses the nonlinear beam column element in the OpenSees software to perform numerical simulation analysis on the RRACFST column. Huang et al. [39] simulated a CFST composite truss girder and lattice pier based on OpenSees software, verifying the accuracy of OpenSees. Cai et al. [40] used OpenSees to analyze the influence of parameters such as steel tube thickness, the axial compression ratio, and the slenderness ratio on the seismic performance of a rectangular ultra-high-performance concrete-filled steel tube (UHPCFST). The nonlinear beam-column element was suitable for the calculation of RRACFST columns. This fiber element discretizes the RRACFS column section into multiple discrete small units without considering the effects of shear deformation and bond slip coefficients, making it consistent with the plane section assumption [41–43]. At the same time, it was assumed that the stress-strain uniaxial distribution and uniformity of the discrete fiber element can be calculated, thereby calculating the relationship between the force and deformation of the entire section. The fiber division of the RRACFST is shown in Figure 16.

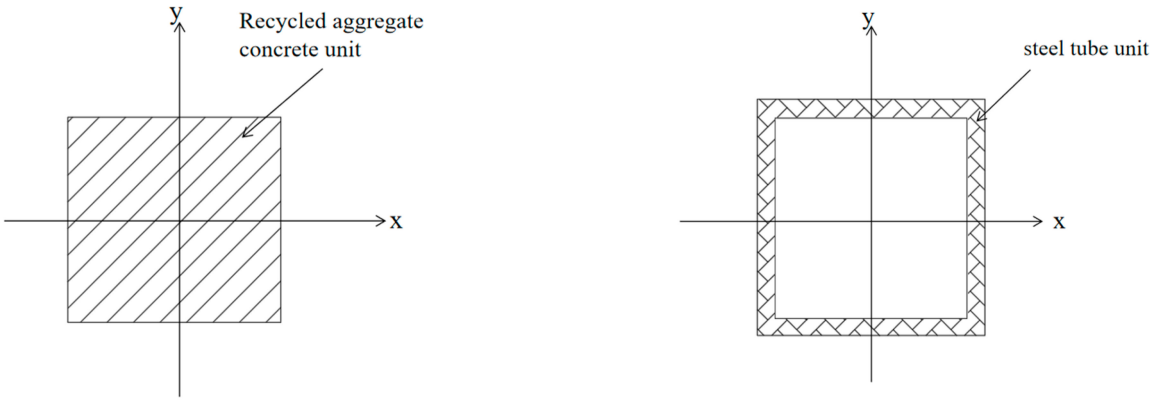


Figure 16. Fiber mesh subdivision.

5. Results

5.1. Comparison of the Hysteresis Curves Between the Experimental and Simulation Curves

The comparison between the measured hysteresis curve of the RRACFST columns and the hysteresis curve calculated by the software OpenSees is shown in Figure 17. It can be seen that the hysteresis curves of all RRACFST columns were relatively full and had good stability, and there was no obvious pinch phenomenon from the early stage to the later stage [44]. At the beginning of the test loading, the hysteresis loop area was relatively long and narrow, and the stiffness of the RRACFST column remained basically unchanged, with weak energy dissipation capacity. After the peak load, due to the increase in residual deformation and decrease in stiffness of the RRACFST column, the hysteresis loop area and energy dissipation performance of the RRACFST column significantly increased, and the curve showed a downward trend, entering the elastic–plastic stage, with the gradual slowing down of its bearing capacity trend. The simulated hysteresis curve had a high degree of agreement with the experimental hysteresis curve, and the positive and negative loading and unloading trends in the early stages of hysteresis curve development were consistent. During the numerical simulation process, the pre-damage RRACFST column yielded a symmetrical simulation result in terms of positive and negative load-bearing capacity, while the pre-damage RRACFST column had varying degrees of deviation in both positive and negative directions, due to the existing residual deformation of the pre-damage RRACFST column. ESJ-confined seismic-damaged RRACFST columns restored the bearing capacity and ductility to levels exceeding their original levels, but the residual strain generated could not be fully restored, resulting in the aforementioned deviation [20]. Especially in the damaged stage of the simulated hysteresis curve, due to the severe impact of the above adverse factors, the calculated hysteresis curve was fuller than the measured hysteresis curve.

5.2. Comparison of Skeleton Curves Between Experimental and Simulation Curves

The comparison between the measured skeleton curve and the simulated skeleton curve of the RRACFST column is shown in Figure 18. It was concluded that the simulated skeleton curve had a high degree of fit with the measured skeleton curve during the elastic stage, indicating that the RRACFST column was in the elastic stage at the beginning of displacement loading, with minimal residual deformation and no plastic hinge, and the bearing capacity increased rapidly [4]. When entering the elastic–plastic stage, the RRACFST column began to show significant residual deformation, the stiffness slope changed, and the bearing capacity growth trend slowed down. This was due to the accumulation of residual deformation, increased energy dissipation capacity, a gradual increase in the plastic hinge, and the fact that the upper and lower ends were not on the same horizontal line. There was an angle between the loading device clamping plate and the RRACFST column, which affected the increase in bearing capacity. During the elastic stage of the skeleton curve, the simulated skeleton curve of the ESJ-confined RRACFST

column "RRACFST-3-T" had a similar accuracy to the measured skeleton curve. Near the peak point, there was a separation between the two but, overall, it was not significant. After reaching the descending section, the simulated skeleton curve and the measured skeleton curve were again close to each other. Among them, the severely seismic-damaged ESJ-confined RRACFST column "RRACFST-3-T" had a high degree of fit in the elastic stage, and in the elastic–plastic stage, the positive and negative bearing capacities of the simulation results were slightly larger than the experimental results. In general, the simulated skeleton curve and the measured skeleton curve agreed well, indicating that although OpenSees software can accurately fit the results, there were differences.

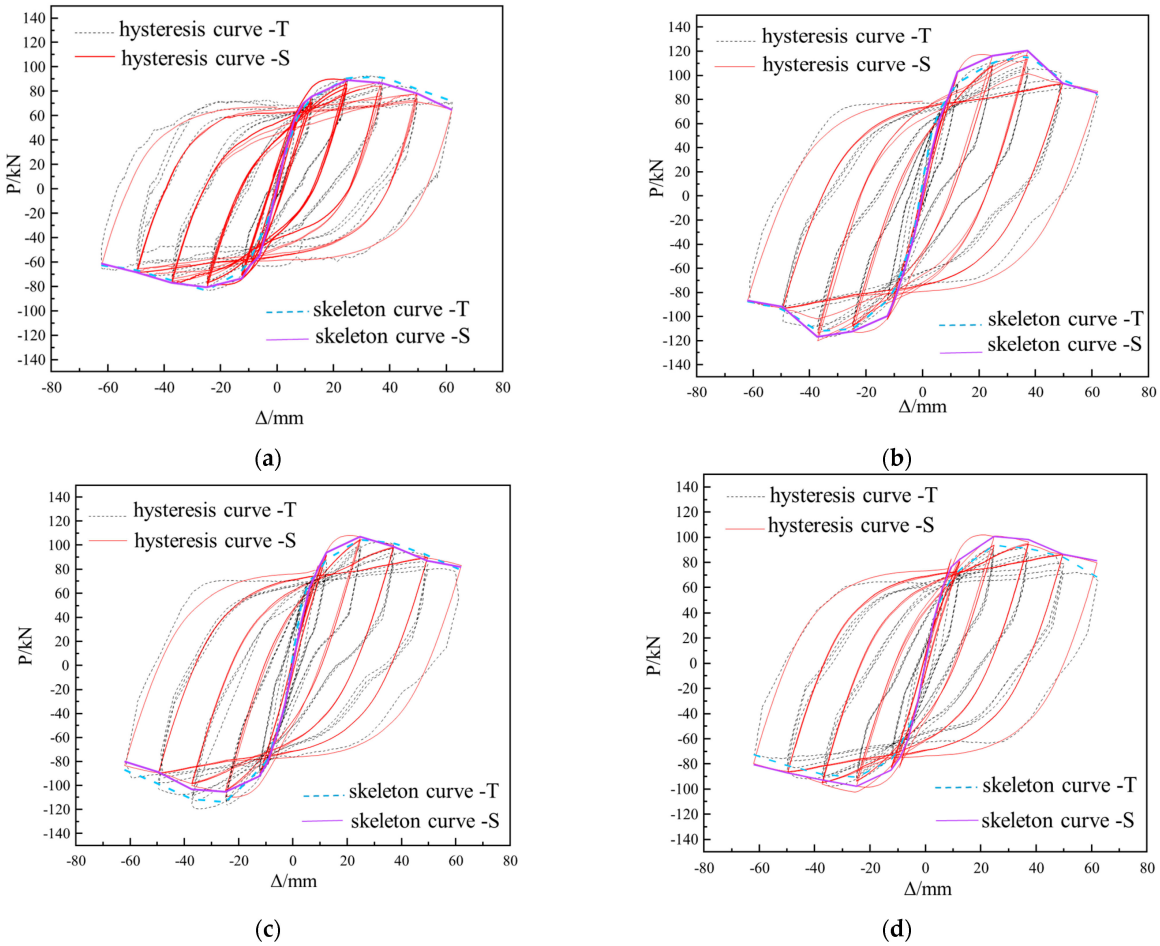


Figure 17. Comparison of the experimental and simulated hysteresis curves. (**a**) RRACFST-0; (**b**) RRACFST-1; (**c**) RRACFST-2; (**d**) RRACFST-3.

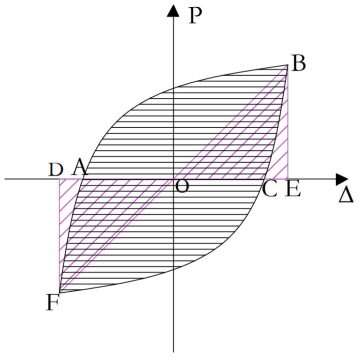


Figure 18. Diagram of the energy dissipation factor.

5.3. Comparison of Bearing Capacity, Ductility, the Simulated Bearing Capacity, and Ductility Between the Experiment and the Simulation

The comparison of the yield point, peak point, and damage point bearing capacities between the test specimen and the simulation is shown in Table 6. It can be concluded that the deviations between the simulated values and the measured values of RRACFST-0 in the three stages were 0.57%, 4.29%, and 4.2%, respectively, and the errors were all controlled to within 5%. The deviation between the measured values and the simulated values of ESJ-confined RRACFST columns increased with the increase in the pre-damage degree of the specimens. The deviation between the specimens without pre-damage and moderate pre-damage was between 3% and 5%, while the deviation between the specimens with severe pre-damage was between 5% and 10%. Overall, the deviation range remained within 5% to 10%, indicating that the residual deformation caused by the pre-damage of the specimens affected the fitting accuracy, and the greater the damage, the greater the impact.

Table 6. Comparison of bearing capacity.

Specimen	Direction	P_y-T (kN)	P_y-S (kN)	P_y-T/P_y-S	P_m-T (kN)	P_m-S (kN)	P_m-T/P_m-S	P_u-T (kN)	P_u-S (kN)	P_u-T/P_u-S
RRACFST-0	Positive	74.2	73.9	1.0042	91.6	86.7	1.0565	77.9	74.2	1.0498
	Negative	67.5	68.5	0.9854	83.4	81.1	1.0283	70.9	70.6	1.0042
	Average	70.8	71.2	0.9943	87.5	83.9	1.0429	74.4	72.4	1.0276
RRACFST-1	Positive	93.6	101.4	0.9329	112.9	120.6	0.9361	93.5	101.4	0.922
	Negative	87.6	91.2	0.9714	117.7	117.2	1.0042	100	98.4	1.0162
	Average	90.6	97.3	0.9511	115.3	118.9	0.9697	96.8	99.9	0.9689
RRACFST-2	Positive	86.5	91.6	0.9443	102.6	106.7	0.9615	86.7	90.3	0.9061
	Negative	80.1	84.4	0.949	116.5	107.6	1.0827	101.6	93.5	1.0866
	Average	83.3	88	0.9465	109.7	107.2	1.0233	94.2	91.9	1.025
RRACFST-3	Positive	73.5	76.4	0.962	93.4	100.7	0.9275	77.7	84.2	0.9228
	Negative	74.5	78.2	0.9526	97.3	97.7	0.9959	82.7	85.4	0.9683
	Average	74.0	77.3	0.9573	95.4	98.7	0.9665	80.2	84.8	0.9457

The formula for calculating the ductility coefficient is shown in Equation (18) [8]:

$$\mu = \Delta_u / \Delta_y. \tag{18}$$

where Δ_u is the damage displacement of the specimen, Δ_y is the yield displacement of the specimen, and μ is the displacement coefficient.

The comparison of the displacement ductility characteristics obtained from the test and simulation is shown in Table 7. It can be concluded that the ductility of the specimen RRACFST-1 was significantly higher than that of the specimen RRACFST-0. This was because the ESJ suppressed the development of buckling in the steel tube. When the steel tube of specimen RRACFST-0 was separated from the core concrete due to buckling, the core concrete inside the steel tube of specimen RRACFST-1 remained in a three-way compression state due to the hoop effect of the ESJ, which delayed the plastic deformation of the core concrete at the plastic hinge and improved its compressive strength and deformation capacity. The ductility coefficients of specimens RRACFST-1 and RRACFST-2 were similar, indicating that the hoop effect of the steel sleeve reduced the impact of seismic damage on the ductility of the specimens. Using steel sleeves to reinforce moderately damaged specimens can significantly improve their deformation capacity. The ductility coefficient of the specimen RRACFST-3 was slightly higher than that of the specimen RRACFST-1, indicating that severe damage had a greater impact on the reinforcement effect of the ESJ. The improvement in its ductility performance was limited, but it could still improve its plastic deformation capacity. Compared with the specimen RRACFST-0, the yield displacement of the reinforced specimen had increased, and its plastic deformation capacity had also improved. The ductility coefficients of the specimens RRACFST-2 and RRACFST-3 were slightly higher than that of the specimen RRACFST-1 after pre-damage, indicating that

the impact of ESJ reinforcement on the ductility coefficient of the component was related to the degree of damage. The higher the degree of damage, the lower the increase in ductility coefficient, and vice versa. After a certain degree of damage, the seismic performance of the reinforced specimen recovered and exceeded that of the pre-damage specimen, and the error between the finite element calculation results and the experimental data was between 2% and 6%, which was relatively accurate.

Table 7. Comparison of the displacement ductility analysis.

Specimen	Direction	Δy-T(kN)	Δy-S(kN)	Δm-T(kN)	Δm-S(kN)	Δu-T(kN)	Δu-S(kN)	*μ-T*	*μ-S*
RRACFST-0	Positive	12.1	11.8	24.9	23.4	43.8	42.2	3.51	3.50
	Negative	12.2	12.3	24.2	24.5	41.4	42.5		
	Average	12.2	12.1	24.6	24.0	42.6	42.4		
RRACFST-1	Positive	12.5	12.8	36.9	36.3	54.9	53.4	4.29	4.10
	Negative	12.7	13.2	37.3	38.4	53.2	53.3		
	Average	12.6	13.0	37.1	37.4	54.1	53.4		
RRACFST-2	Positive	12.4	12.6	33.6	28.7	50.6	48.5	4.15	3.91
	Negative	12.4	12.5	35.2	33.1	52.3	49.7		
	Average	12.4	12.6	34.4	30.9	51.5	49.1		
RRACFST-3	Positive	12.2	12.4	27.1	27.3	46.6	45.9	3.76	3.67
	Negative	12.3	12.2	27.4	26.8	45.4	44.3		
	Average	12.3	12.3	27.3	27.1	46.0	45.1		

5.4. Comparison of the Energy Dissipation Capability Between the Experiment and the Simulation

The energy dissipation capacity of the specimen was measured by calculating the area within the hysteresis curve, then the energy dissipation capacity of the specimen was evaluated. The calculation formula is as follows [11]:

$$E = \frac{S_{(ABC + CFA)}}{S_{(OBE + ODF)}} \tag{19}$$

where $S_{ABC} + S_{CFA}$ represents the area of the hysteresis loop, and $S_{OBE} + S_{ODF}$ represents the area of the triangle corresponding to the peak point of the hysteresis loop, as shown in Figure 18.

The comparison between the measured energy dissipation capacity and the simulation in the test are mainly reflected in Table 8, showing the values after the RRACFST column entered the elastic–plastic stage. The results showed that the deviation between the measured energy dissipation capacity and the simulated energy dissipation capacity of all RRACFST columns during the damaged stage was within the range of 5–10%. The simulated energy dissipation capacity of RRACFST-0 was lower than that of the ESJ-confined RRACFST columns, which can improve the energy dissipation capacity of the RRACFST column. The ESJ reinforcement participated in the early stress seen in the steel tube, and the measured energy dissipation capacity and simulated energy dissipation capacity of the RRACFST column RRACFST-3 were both within the range of 10–15% at the peak stage. The deviation between the measured energy dissipation capacity and the simulated energy dissipation capacity of RRACFST-2 at the peak stage was within the range of 5–10%, which was due to its pre-damage degree being less than that of the severely pre-damaged RRACFST column, indicating that the degree of pre-damage affected the fitting accuracy. The greater the degree of pre-damage, the greater the error in fitting accuracy.

5.5. Comparison of the Stiffness Capacity Degradation Between the Experiment and the Simulation

Under the same displacement conditions, the stiffness of the specimen degraded under the action of reciprocating loads, and the ability of the specimen to resist horizontal loads also became increasingly poor [4,44]. Therefore, when studying the seismic performance of ESJ-confined RRACFST columns through testing and simulation, the stiffness of the

specimen should also be considered. The stiffness degradation curve calculation formula is as follows [10]:

$$K_j = \frac{\left|+F_j^i\right| + \left|-F_j^i\right|}{\left|+X_j^i\right| + \left|+X_j^i\right|} \tag{20}$$

The stiffness degradation curves of all test specimens were plotted together, and the test results were compared with the finite element results, as shown in Figure 19. It can be seen that the test results matched well with the finite element results. The test and simulation results showed that as the horizontal displacement increased, the secant stiffness of each specimen before yielding decreased rapidly, and after yielding, the stiffness decreased slowly. The secant stiffness of the reinforced specimens before yielding was much higher than that of the comparison specimens, indicating that ESJ reinforcement can significantly improve the initial stiffness of the specimens. Throughout the loading process, the stiffness was higher than that of the comparison specimens, indicating that ESJ reinforcement can also effectively delay the stiffness degradation of the specimens. The stiffness degradation curves of the reinforced specimens from high to low were RRACFST-1, RRACFST-2, and RRACFST-3, indicating that the stiffness of the reinforced specimens was affected by the degree of pre-damage of the specimens. The greater the degree of damage, the faster the stiffness degradation. The secant stiffness of RRACFST-3 and RRACFST-0 was similar, and the stiffness increase was small, indicating that ESJ reinforcement offered limited improvement in the stiffness of severely damaged specimens. The fitting degree of the test and simulated degradation stiffness curves decreased with increasing damage degree but, overall, the test curve fitted well, indicating the accuracy of the finite element analysis.

Table 8. Comparison of energy dissipation.

Specimen	Peak Period	Proportion	Disruption Phase	Proportion
RRACFST-0-T	1.18	0.91	2.43	0.96
RRACFST-0-S	1.32		2.52	
RRACFST-1-T	1.68	0.94	2.89	1.04
RRACFST-1-S	1.78		2.80	
RRACFST-2-T	1.65	0.94	2.84	0.99
RRACFST-2-S	1.76		2.85	
RRACFST-3-T	1.29	0.81	2.75	1.05
RRACFST-3-S	1.62		2.63	

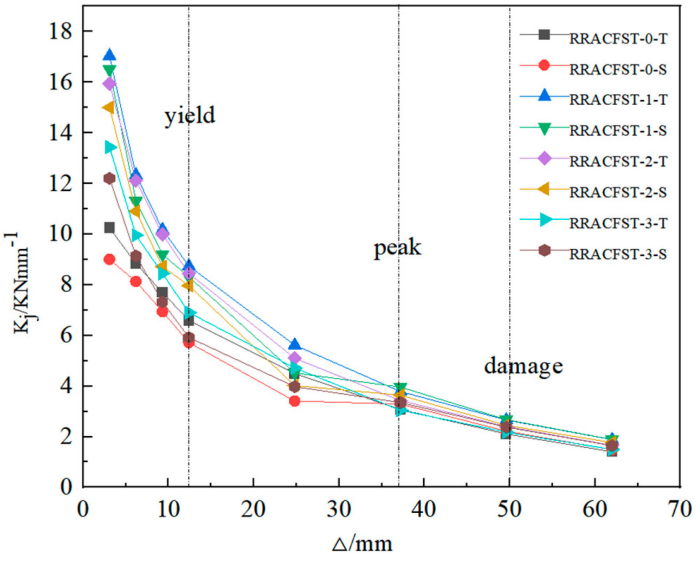


Figure 19. Comparison of the stiffness degradation curves.

In conclusion, the simulated hysteresis curve and skeleton curve had a high degree of agreement with the experimental hysteresis curve and skeleton curve. The error in bearing capacity, ductility, energy dissipation ability, and stiffness degradation ability was small. This indicated that the selected material's constitutive, parameter setting, and calculation methods through OpenSees are more suitable for modeling and calculating RRACFST frame columns.

6. Parametric Analysis

Figure 20 shows the skeleton curves of severely seismic-damaged ESJ-confined columns for different RAC strengths, recycled coarse aggregate replacement rates, steel grade, steel tube thickness, axial compression ratios, and slenderness ratios. As shown in Figure 20a, when the replacement rate of the recycled coarse aggregate gradually increased, the elastic phase of the skeleton curve was not obvious. The impact on the stiffness of the specimen in the elastic phase was small and the fluctuation in the descending segment of the skeleton curve was small, basically remaining consistent. However, at the peak point, the defect performance was relatively obvious, and the peak bearing capacity of each specimen varied by 3.42%, 1.17%, −0.82%, and −0.18%, with differences of less than 5%. It was found that the peak load of the specimen decreased rapidly when the replacement rate of the recycled coarse aggregate was not less than 50%; thus, it is recommended that the replacement rate of recycled coarse aggregate should not be less than 50%. The higher the RAC strength, the greater the peak load of the specimen. As shown in Figure 20b, considering engineering economic factors, it is recommended to use RAC with high cost performance, rather than high-strength RAC, and it is recommended that the strength of the RAC in RRACFST frame columns should be C40. As shown in Figure 20c, when the axial compression ratio was between 0 and 0.5, the peak bearing capacity of the specimen varied within 5%. When the axial compression ratio was greater than 0.5, the peak bearing capacity of the specimen varied from 5% to 10%. When the axial compression ratio was 0 and 0.1, the skeleton curve of the specimen only showed a slight downward trend until the axial compression ratio reached 0.3, when the downward trend in the skeleton curve became more pronounced. When the axial compression ratio was 0.7, the peak load of the specimen appeared to be one displacement stage ahead, and the bearing capacity of the specimen decreased significantly, with a decrease in ductility and a change in the overall trend of the skeleton curve. It is recommended that the axial compression ratio of severely seismic-damaged ESJ-confined RRACFST columns should be 0.3. As shown in Figure 20d, when the steel was upgraded from Q235 to Q420, the peak load of the specimen increased by 15.65%, 10.02%, and 4.10%, respectively. It was found that the Q345 grade steel showed the largest increase in strength, and it is recommended to choose Q345 grade steel. As shown in Figure 20e, the peak load of the specimens increased by 32.6%, 21.2%, 18.9%, and 14.4%, respectively, when the steel thickness increased from 2 mm to 6 mm, and it was found that the increase effect of a steel tube thickness of 4 mm was better. In Figure 20f, the peak load of the specimens increased by 11.7%, −20.2%, and −19.6%, respectively, indicating that the slenderness ratio cannot be ignored in the seismic performance of severely seismic-damaged ESJ-confined RRACFST columns, and it is recommended that the slenderness ratio should be 7.5.

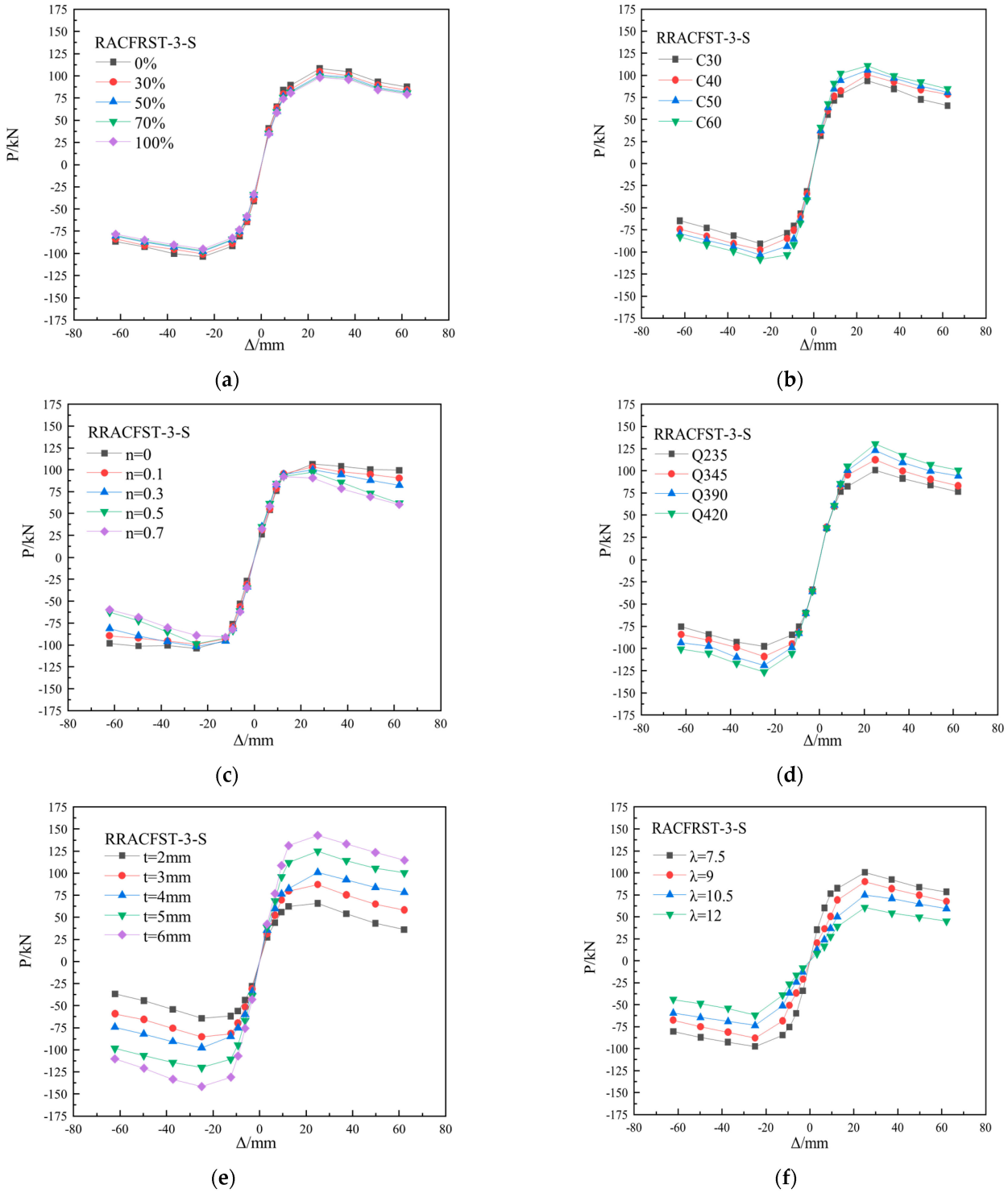


Figure 20. Effect of different parameters on ESJ-confined severely seismic-damaged RRACFST columns. (**a**) Comparison of recycled coarse aggregate replacement rates. (**b**) Comparison of RAC strength. (**c**) Comparison of axial compression ratios. (**d**) Comparison of steel strength. (**e**) Comparison of steel thickness. (**f**) Comparison of slenderness ratios.

7. Conclusions

Based on existing experimental research, this article established a correct and suitable model for ESJ-confined seismic-damaged RRACFST columns using OpenSees software. The authors have conducted research on the seismic performance and seismic parameter analysis of ESJ-confined seismic-damaged RRACFST columns and propose a suitable restor-

ing force model and optimal combination of seismic parameters. The main conclusions are as follows:

(1) Based on the hysteresis curve obtained from the experimental data, comprehensive feature points, fixed point determination, bearing capacity reduction, and softening point processing, a trilinear skeleton curve model and a restoring force model were proposed, and the hysteresis rules were given. The results showed that the curve calculated by the restoring force model was in good agreement with the measured hysteresis curve in the experiment, proving the feasibility of such restoring force models, which provide a reference for the use and design of elastoplastic analyses of such components under seismic action.

(2) The simulation results were in good agreement with the experimental results. The hysteresis curves were full and stable, and the skeleton curves were relatively complete and similar in shape. This indicates that the steel and concrete constitutive models and fiber elements selected for the RRACFST columns had good applicability and can provide a reference for subsequent RRACFST column calculations.

(3) The higher the pre-damage degree of the RRACFST column, the greater the error between the simulation results and the measured curve, but the error range remains within 5–15%, indicating that the degree of pre-damage affects the accuracy of curve fitting.

(4) For ESJ-confined RRACFST columns, a comparative simulation analysis was conducted on their bearing capacity, displacement ductility, stiffness degradation, and energy dissipation capacity. The ESJ reinforcement participated in the early stress of the steel tube, and the ESJ reinforcement provided effective reinforcement. Based on the open-source software OpenSees, a parametric analysis was conducted on the pre-damage specimens, and further research on such structures showed that when the replacement rate of recycled coarse aggregate was 50%, the concrete strength was C40, the axial compression ratio was 0.3, the strength of the rectangular steel tube was Q345, the wall thickness of the steel tube was 4 mm, and the slenderness ratio was 7.5, the components were more in line with economic and engineering application requirements.

(5) This article proposes a restoring force correction model for enveloped steel jacket-confined seismic-damaged rectangular recycled aggregate concrete-filled steel tubular columns, which can used to provide a theoretical basis for elastoplastic analysis.

Author Contributions: J.Y.: Data curation, formal analysis, writing—original draft, visualization, and investigation. N.C. and Y.S.: Conceptualization, funding acquisition, writing—review and editing, and supervision. S.P. and T.W.: Formal analysis and investigation. All authors have read and agreed to the published version of the manuscript.

Funding: This research is funded by the 'Natural Science Foundation of Hubei Province (CN)'—'China' (Grant No. 2022CFB662), 'Tianjin Key Laboratory of Building Green Functional Materials of China (CN)'—'China' (Grant No. JZ-2023003), 'State Key Laboratory of Precision Blasting and Hubei Key Laboratory of Blasting Engineering, Jianghan University (CN)'—'China' (Grant No. PBSKL2022D05), and their support is gratefully acknowledged.

Data Availability Statement: The authors are unable to or have chosen not to specify which data have been used.

Conflicts of Interest: Author Jun Yan was employed by the company Wuhan Bohong Construction Group Co., Ltd. The remaining authors declare that the research was conducted in the absence of any commercial or financial relationships that could be construed as a potential conflict of interest.

References

1. Zhang, X.G.; Gao, X. The hysteretic behavior of recycled aggregate concrete-filled square steel tube columns. *Eng. Struct.* **2019**, *198*, 109523. [CrossRef]
2. Kurda, R.; de-Brito, J.; Silvestre, J.D. Combined influence of recycled concrete aggregates and high contents of fly ash on concrete properties. *Constr. Build. Mater.* **2017**, *157*, 554–572. [CrossRef]
3. Kwan, W.H.; Ramli, M.; Kam, K.J.; Sulieman, M.Z. Influence of the amount of recycled coarse aggregate in concrete design and durability properties. *Constr. Build. Mater.* **2012**, *26*, 565–573. [CrossRef]

4. Ozkilic, Y.O.; Madenci, E.; Mansour, W.; Sharaky, I.A.; Fayed, S. Behavior of self-compacting recycled concrete filled aluminum tubular columns under concentric compressive load. *Steel Compos. Struct.* **2024**, *51*, 243.
5. Fayed, S.; Madenci, E.; Özkiliç, Y.O.; Mansour, W. Improving bond performance of ribbed steel bars embedded in recycled aggregate concrete using steel mesh fabric confinement. *Constr. Build. Mater.* **2023**, *369*, 130452. [CrossRef]
6. Fayed, S.; Madenci, E.; Özkiliç, Y.O.; Tawfik, T.A. Effect of block size on bearing strength of steel fiber-reinforced recycled aggregate concrete. *Arab. J. Sci. Eng.* **2023**, *49*, 5287–5303. [CrossRef]
7. Di Cesare, A.; Belviso, P.; Ponzo, F.C.; Vitone, G. Seismic behavior and modeling of ductile composite steel-trussed concrete beam to column joints. *Appl. Sci.* **2023**, *13*, 11139. [CrossRef]
8. Colajanni, P.; La Mendola, L.; Monaco, A.; Pagnotta, S. Low-damage friction connections in hybrid joints of frames of reinforced concrete buildings. *Appl. Sci.* **2023**, *13*, 7876. [CrossRef]
9. Colajanni, P.; La Mendola, L.; Monaco, A.; Pagnotta, S. Seismic performance of earthquake-resilient RC frames made with HSTC beams and friction damper devices. *J. Earthq. Eng.* **2022**, *26*, 7787–7813. [CrossRef]
10. Dong, H.; Qin, J.; Chen, Z.; Cao, W.; Tang, Y. Seismic behavior of full-scale square high-strength RACFST columns. *Structures* **2021**, *34*, 2600–2616. [CrossRef]
11. Liu, Z. Experimental and numerical study on seismic performance of steel reinforced concrete spatial frame with irregular section columns. *Eng. Struct.* **2021**, *242*, 112507. [CrossRef]
12. Bicici, E.; Sezen, H. Cyclic shear displacement model for reinforced concrete columns. *Eng. Struct.* **2021**, *247*, 113211. [CrossRef]
13. Liu, C.; Wang, Y.; Wang, W.; Wu, X. Seismic performance and collapse prevention of concrete-filled thin-walled steel tubular arches. *Thin-Walled. Struct.* **2014**, *80*, 91–102. [CrossRef]
14. Sundarraja, M.C.; Ganesh-Prabhu, G. Experimental study on CFST members strengthened by CFRP composites under compression. *J. Constr. Steel. Res.* **2012**, *72*, 75–83. [CrossRef]
15. Fang, L.; Zhang, B.; Jin, G.F.; Li, K.W.; Wang, Z.L. Wang, Seismic behavior of concrete-encased steel cross-shaped columns. *J. Constr. Steel. Res.* **2015**, *109*, 24–33. [CrossRef]
16. Giménez, E.; Adam, J.M.; Ivorra, S.; Calderón, P.A. Influence of strips configuration on the behavior of axially loaded RC columns strengthened by steel angles and strips. *Mater. Design.* **2009**, *30*, 4103–4111. [CrossRef]
17. Nagaprasad, P.D.; Sahoo, R.; Rai, D.C. Seismic strengthening of RC columns using external steel cage. *Earthquake. Eng. Struct. Dyn.* **2010**, *38*, 1563–1586. [CrossRef]
18. Garzón-Roca, J.; Ruiz-Pinilla, J.; Adam, J.M.; Calderón, P.A. An experimental study on steel-caged RC columns subjected to axial force and bending moment. *Eng. Struct.* **2011**, *3*, 580–590. [CrossRef]
19. Xu, C.-X.; Peng, S.; Deng, J.; Wan, C. Study on seismic behavior of encased steel jacket-strengthened earthquake-damaged composite steel-concrete columns. *J. Build. Eng.* **2018**, *17*, 154–166. [CrossRef]
20. Aldhafairi, F.; Hassan, A.; Abd-El-Hafez, L.; Abouelezz, A. Different techniques of steel jacketing for retrofitting of different types of concrete beams after elevated temperature exposure. *Structures.* **2020**, *28*, 713–725. [CrossRef]
21. Peng, S.; Liu, G.; Xiong, Z.; Wang, J.; Li, G. Effect of confinement materials and damage degree on the seismic behavior of RACFST columns. *J. Build. Eng.* **2022**, *57*, 104938. [CrossRef]
22. Di Trapani, F.; Malavisi, M.; Marano, G.C.; Sberna, A.P.; Greco, R. Optimal seismic retrofitting of reinforced concrete buildings by steel-jacketing using a genetic algorithm-based framework. *Eng. Struct.* **2020**, *219*, 110864. [CrossRef]
23. Xue, J.Y.; Yang, Y.; Qi, L.J. Restoring force model of steel-reinforced recycled concrete frames infilled with recycled concrete blocks. *J. Build. Eng.* **2020**, *60*, 105173. [CrossRef]
24. Han, L.H.; Huang, H.; Zhao, X.L. Analytical behavior of concrete-filled double skin steel tubular(CFDST) beam-columns under cyclic loading. *Thin-Walled. Struct.* **2009**, *47*, 668–680. [CrossRef]
25. Peng, S.; Xiong, Z.; Zeng, X. A restoring force model for CFRP seismic-damaged RACFST columns: Theoretical, experimental, and simulation analysis. *Structures* **2022**, *40*, 273–283. [CrossRef]
26. Wang, K.; Lu, X.-F.; Yuan, S.-F.; Cao, D.-F.; Chen, Z.-X. Analysis on hysteretic behavior of composite frames with concrete-encased CFST columns. *J. Constr. Steel. Res.* **2017**, *135*, 176–186. [CrossRef]
27. Wu, C.L.; Liu, X.; Pan, W.; Mou, B. Restoring force model for modular prefabricated steel-reinforced concrete column to H-shaped steel beam composite joints. *J. Build. Eng.* **2021**, *42*, 102845. [CrossRef]
28. Yun, C.; Chao, C.; Cong, C. Study on seismic performance of prefabricated self-centering beam to column rotation friction energy dissipation connection. *Eng. Struct.* **2021**, *241*, 112136. [CrossRef]
29. *JGJ/T 101-2015*; Specification for Seismic Test of Buildings. China Academy of Building Research: Beijing, China, 2015.
30. *GB 50011-2010*; Code for Seismic Design of Buildings. China National Institute of Standardization: Beijing, China, 2010.
31. Hu, X.W.; Ding, R.; Zhang, Z.Y.; Fan, J.S. A unified section-based restoring force model for reinforced concrete coupling beams based on the XGBoost model: Establishment, validation and application. *J. Build. Eng.* **2023**, *73*, 106666. [CrossRef]
32. Du, Y.S. Seismic behavior of CFRP confined rectangular CFST columns using high-strength materials: Numerical analysis and restoring force model. *Structures* **2021**, *34*, 4237–4253. [CrossRef]
33. Hu, S.; Zhou, L.; Cheng, H.; Liu, S. Restoring force model of phosphogypsum-filled cold-formed thin-walled square steel tube composite wall. *Structures* **2024**, *65*, 106732. [CrossRef]
34. Rodrigues, H. Simplified hysteretic model for the representation of the biaxial bending response of RC columns. *Eng. Struct.* **2012**, *44*, 146–158. [CrossRef]

35. Xiao, J.Z.; Huang, X.; Shen, L.M. Seismic behavior of semi-precast column with recycled aggregate concrete. *Construct. Build. Mater.* **2012**, *35*, 988–1001. [CrossRef]
36. Sivaselvan, M.V.; Reinhorn, A.M. Hysteretic models for deteriorating inelastic structures. *J. Eng. Mech.* **2000**, *126*, 633–640. [CrossRef]
37. Tang, Y.C. Seismic performance evaluation of recycled aggregate concrete-filled steel tubular columns with field strain detected via a novel mark-free vision method. *Structures* **2022**, *37*, 426–441. [CrossRef]
38. Yu, M.; Zha, X.; Ye, J.; Li, Y. A unified formulation for circle and polygon concrete-filled steel tube columns under axial compression. *Eng. Struct.* **2013**, *49*, 1–10. [CrossRef]
39. Huang, Y.; Briseghella, B.; Zordan, T.; Wu, Q.; Chen, B. Shaking table tests for the evaluation of the seismic performance of an innovative lightweight bridge with CFST composite truss girder and lattice pier. *Eng. Struct.* **2014**, *75*, 73–86. [CrossRef]
40. Cai, H. Seismic performance of rectangular ultra-high performance concrete filled steel tube (UHPCFST) columns. *Compos. Struct.* **2020**, *259*, 113242. [CrossRef]
41. Ahmed, M.; Ci, J.; Yan, X.-F.; Lin, S.; Chen, S. Numerical modeling of axially loaded circular concrete-filled double-skin steel tubular short columns incorporating a new concrete confinement model. *Structures* **2021**, *30*, 611–627. [CrossRef]
42. Ahmed, M.; Ci, J.; Yan, X.F.; Chen, S. Nonlinear analysis of elliptical concrete-filled stainless steel tubular short columns under axial compression. *Structures* **2021**, *32*, 1374–1385. [CrossRef]
43. Ahmed, M.; Liang, Q.Q. Numerical analysis of thin-walled round-ended concrete-filled steel tubular short columns including local buckling effects. *Structures* **2020**, *220*, 181–196. [CrossRef]
44. Fayed, S.; Aksoylu, C.; Ecemiş, A.S.; Madenci, E.; Özkılıç, Y.O. Tensile behavior of green concrete made of fine/coarse recycled glass and recycled concrete aggregates. *Buildings* **2024**, *14*, 2969. [CrossRef]

Disclaimer/Publisher's Note: The statements, opinions and data contained in all publications are solely those of the individual author(s) and contributor(s) and not of MDPI and/or the editor(s). MDPI and/or the editor(s) disclaim responsibility for any injury to people or property resulting from any ideas, methods, instructions or products referred to in the content.